Advances in Geo-Energy Research

Vol. 12, No. 3, p. 183-193, 2024

Original article

Failure patterns in layered gas-storage systems

Zhenqi Guo[1,3], Xiangbo Gao[1,3], Huanyu Wu[4], Lei Liu[1,3], Liang Lei[2,3,5]*

[1]*College of Environmental and Resources Science, Zhejiang University, Hangzhou 310058, P. R. China*

[2]*Research Center for Industries of the Future, Westlake University, Hangzhou 310030, P. R. China*

[3]*Key Laboratory of Coastal Environment and Resources of Zhejiang Province, School of Engineering, Westlake University, Hangzhou 310030, P. R. China*

[4]*Department of Civil and Environmental Engineering, The Hong Kong Polytechnic University, Hong Kong 999077 SAR, P. R. China*

[5]*Institute of Advanced Technology, Westlake Institute for Advanced Study, Hangzhou 310024, P. R. China*

Keywords:
Layered gas-storage system
failure pattern
gas invasion behavior
X-ray CT

Cited as:
Guo, Z., Gao, X., Wu, H., Liu, L., Lei, L. Failure patterns in layered gas-storage systems. Advances in Geo-Energy Research, 2024, 12(3): 183-193. https://doi.org/10.46690/ager.2024.06.03

Abstract:
The underground storage of gases, such as CO_2 and H_2, in the porous media is a critical component for achieving carbon neutrality and economical energy storage. While previous research has predominantly focused on gas injection in one piece of uniform porous media, and gravity is often neglected, the reality is that natural storage formations are typically multi-layered porous systems. An in-situ gas injection apparatus based on high-resolution micro-CT was utilized to investigate gas injection behaviors and failure patterns in layered porous media systems. The system includes a reservoir layer and a cap layer, where both capillarity and permeability are meticulously controlled. Our findings reveal that all cases experience cycles of a pressure built-up period and a sudden pressure release when a barrier, either capillarity or effective stress, is overcome. Drainage conditions within the layered system significantly impact both the volume of gas trapped and the failure patterns observed. Effective stress analyses show that the key determinants of failure patterns are capillarity, effective stress, and excess pore fluid pressure, affected by pore size, cap layer thickness, gas injection rate and permeability. Five distinct failure patterns are categorized: capillary invasion, fracture opening, integral uplifting, local heaving, and violent liquefaction-based on two dimensionless parameters. This work provides new insights into understanding the gas injection dynamics in layered porous media.

1. Introduction

Gas injection into geological settings, and the subsequent trapping-storage or leakage, play a significant role in both natural and engineering environments. Such processes contribute to the formation of phenomena like shallow gassy sediments in both marine and permafrost environments, in addition to the well-known methane seeps, gas-mud diapir structures and pockmarks (Brooks et al., 1986; Hovland, 1992; Chiu et al., 2006; Szpak et al., 2015; Lu et al., 2017; Shakhova et al., 2017; Mazzini et al., 2023). Furthermore, in engineering applications, these processes are pivotal in enhanced oil recovery, landfill operation, soil remediation, and underground gas storage (Vidonish et al., 2016; Teng and Zhang, 2018; Blunt and Lin, 2022; Phukan and Saha, 2022; Li and Cai, 2023). Especially, carbon dioxide (CO_2) geological sequestration, as one type of gas storage, draws increasing attention for its potential to reduce the greenhouse effect (Espinoza and Santamarina, 2010; Huppert and Neufeld, 2014; Ranaee et al., 2022; Hematpur et al., 2023; Zhang et al., 2023a). Therefore, it is imperative to understand the mechanisms and interaction between gas and water in the pores and its influence on the porous media skeleton (Fauria and Rempel, 2011; Reynolds and Krevor, 2015; Blunt, 2017; Zhang et al., 2023b; Qin et al., 2024; Zou et al., 2024).

In rigid porous media, displacement mechanisms of immiscible fluids have been extensively studied through both laboratory experiments and computer-based simulations (Saffman, 1986; Lenormand et al., 1988; Fernández

Yandy Scientific Press

*Corresponding author.
E-mail address: guozhenqi@westlake.edu.cn (Z. Guo); gaoxiangbo@westlake.edu.cn (X. Gao); huanyu.wu@connect.polyu.hk (H. Wu); liulei84@westlake.edu.cn (L. Liu); leiliang@westlake.edu.cn (L. Lei).

Received April 12, 2024; revised April 30, 2024; accepted May 18, 2024; available online May 26, 2024.

Table 1. Details in layered system preparation.

Layer	Specimen case number	Grain size range (mm)	Thickness (mm)	Waterhead (mm)	Total weight (g)
Cap	C1	0.075 ~ 0.15	/	/	/
	C2	0.15 ~ 0.30	/	/	/
	C3	0.30 ~ 0.60	20	/	13.1
	C4	0.60 ~ 1.18	/	165	/
	C5	1.18 ~ 2.36	/	/	/
Intermediate reservoir	/	0.10 (mean size)	< 0.15	/	2.1
	/	2.36 ~ 4.75	60	/	78.8

et al., 1991; Ferer et al., 2004; Toussaint et al., 2005; Liu et al., 2013; Cai et al., 2021). Different invasion patterns, including stable displacement, capillary fingering and viscous fingering, have been suggested to be influenced by the fluid flow velocity, pore structures, the viscosity ratio between fluids, ratios between capillary and viscous forces and between gravitational and capillary forces.

In a deformable media, gas migration can displace grains and alter the pore structure (Saffman and Taylor, 1958; Chevalier et al., 2009; Huang et al., 2012; Saintyves et al., 2013; Oppenheimer et al., 2015; Varas et al., 2015; Cai et al., 2024). Such alterations subsequently influence gas flow patterns. Factors like gas entering pressure, capillary pressure, and effective stress can lead to invasion patterns, such as gas-driven fractures (Jain and Juanes, 2009; Holtzman et al., 2012; Campbell et al., 2017; Sun and Santamarina, 2019) and stick-slip bubbles (Sandnes et al., 2011).

Most previous studies use Hele-Shaw cells by simply injecting gas with pumps, considered as two-dimensional (2D) or quasi-2.5D, without explaining the driving forces, and few studies examine the gas invasion process in three-dimensional (3D) or consider the effect of gravity. Techniques like X-ray CT provide a non-destructive insight into gas behaviors at the pore scale (Barry et al., 2010; Zhou et al., 2010; Choi et al., 2011; Mahabadi et al., 2018). In addition, these studies start with homogeneous and isotropic porous media, while the heterogeneity and anisotropy in natural geological structures (Xue et al., 2006; Ranaee et al., 2022), may affect pore pressure dissipation and lead to crack formation, as suggested by field observations (Vidal-Gilbert et al., 2010; Sultan et al., 2020). This variability in structural properties can lead to non-uniform stress distributions during fluid injection (Eyinla et al., 2023). To the best of our knowledge, there is no study on multi-layered systems, and gravity is seldom considered. Furthermore, when the system deviates from mechanical equilibrium, excess pore water pressure Δu, first introduced to soil mechanics by Terzaghi (1943), often referred to as overpressure in geology, becomes significant. The term "overpressure" varies across different disciplines (Peacock et al., 2017) and generally refers to the pore fluid pressure without differentiating gas and water pressure.

This study considers the natural layered systems as a series of two-layered systems and aim to extract universal rules in the simplified two-layer systems with a reservoir layer and a cap layer. An in-situ gas injection device based on high-resolution CT imaging was utilized to visualize gas invasion behavior in the reservoir layer and failure in the cap layer. Results indicate that during the invasion process within the reservoir layer, the drainage conditions and the associated excess pore fluid pressure significantly affect the trapped gas volume and variations in the effective stress. Moreover, a phase diagram using two dimensionless parameters is introduced to categorize the failure patterns of the cap layer.

2. Experimental setup and method

Here, natural conditions within a layered system submerged in water are emulated, featuring a cap layer and a reservoir layer beneath. Consider a gas source gradually invading into the reservoir layer, corresponding to the gas migration from the faults (Hustoft et al., 2007; Ostanin et al., 2012). Our objective is to investigate the response of the layered system during the gas invasion process.

2.1 The composition of the layered system

The controlling factor for the cap layer is the ratio between capillary barrier P_c^* (related to pore/particle size) and effective stress σ' (thickness related self-weight). In our experiments, particle sizes are varied (Table 1) while maintaining a consistent layer thickness. Specifically, the particle size in the reservoir layer is purposely selected large so that the capillarity would allow for a flat gas-water interface at the bottom of the gas pocket (2.36 ~ 4.75 mm in diameter, about 1.3 mm of capillary rise as measured). There are cases in which the selected particle size in the cap layer is too small compared to the reservoir layer, which risks top particles descending into the bottom pores, necessitating the addition of an intermediate layer. A detailed setup schematic can be found in Fig. 1.

2.2 Specimen preparation, boundary conditions and gas injection procedure

First, the acrylic glass tube is filled with a 40 mm depth of 5 wt% potassium iodide (KI) solution, with KI added as an enhancing agent to better separate pore water and pore gas in CT images (Lei et al., 2018). Then, coarse sands are divided into ten batches and added to the tube. A stirring rod is applied

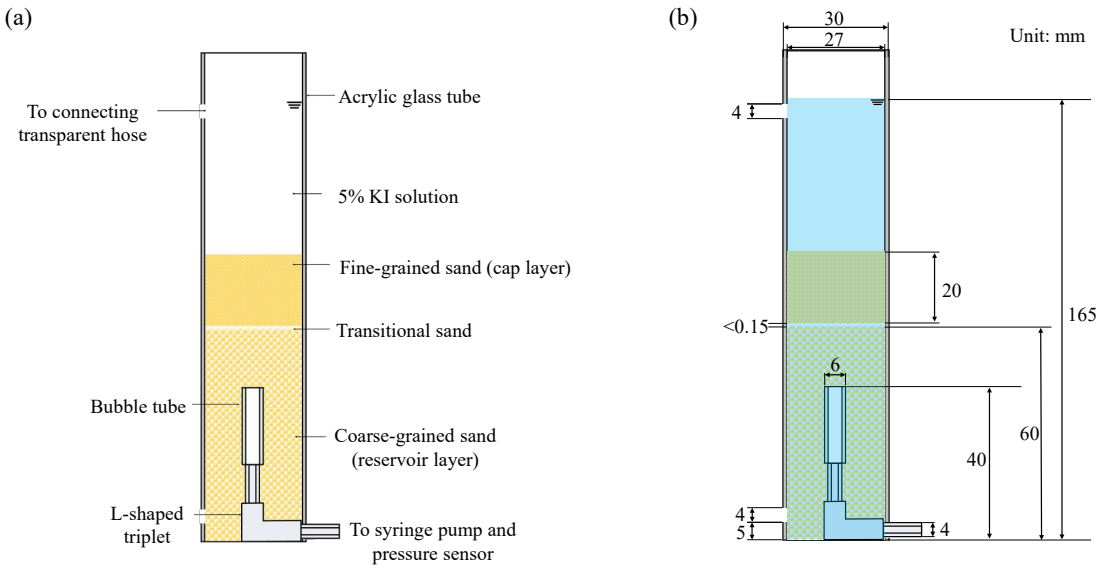

Fig. 1. Schematic of (a) the layered system and (b) detailed design.

to eliminate potential bubbles adhering to the sand particle surface. Often, a few tiny bubbles are found later, but their impact is considered small on the pore water saturation and gas-water interaction. Next, the intermediate layer particles are carefully placed in the surface pores of the coarse sand by a tweezer one by one, roughly 0.15 mm in thickness. Finally, fine sands are added to form the 20-mm-thick cap layer.

Consider the ratio between the gas invasion and pore fluid drainage rate could vary in a natural boundary condition. A hose is implemented to connect the reservoir layer and the top water layer, mimicking a well-drained condition. When the hose is not connected, the drainage has to go through the cap layer, which could be much slower; in extreme cases, the gas pocket can break the connection between the up and bottom pore fluid, resulting in an undrained condition.

A syringe pump is employed to consistently control the gas injection rate across experiments. Gas injection rates are varied among 0.03, 0.06, 0.12, 0.24, 0.48, 0.96 and 1.92 mm/s (equivalent to injection volume rates of 25 to 1,600 mm^3/s).

2.3 Observation and micro-CT scan

The observation apparatus comprises a digital camera, a micro-CT, and a pressure sensor. The pore pressure signal is recorded every second, and the experimental apparatus is illustrated in Fig. 2(a). A series of CT scanning points is employed to gain insights into the pore scale behaviors. These points are designed to capture system reactions at main stages during a constant gas injection (further discussion in Section 3.1). The CT images are segmented (Fig. 2(b)) by a machine learning method (Sommer et al., 2011), and quantitative analyses and volume rendering are facilitated by software tools like Avizo (VSG Inc.) and ImageJ (Rueden et al., 2017).

3. Results and discussion

In this section, the impact of drainage conditions on gas invasion behaviors and the volume of gas trapped within the reservoir layer is initially examined. Subsequent analysis focuses on the effective stress associated with various failure patterns in the cap layer, alongside calculations of the excess pore fluid pressure resulting from rapid gas injection rates. Finally, the discussion is generalized by introducing two dimensionless parameters that define the failure pattern of the cap layer.

3.1 The drainage effect

The concept of a drained condition refers to the scenario where the original pore fluid remains effectively connected to the free water table, preventing the buildup of excess pore fluid pressure during gas injection. In this context, the key balance is between the maximum capillarity the pore structure can hold P_c^* and the local effective stress σ'. First, specimen C1 (Table 1) is considered, with a high P_c^*/σ' ratio for the cap layer. The gas injection rate is relatively low at 0.025 mm^3/s so that at each time point the system is considered at mechanical equilibrium. The pressure variations in response to injection time are depicted in Fig. 3(a). The injection process can be divided into four stages (S1 to S4). Stage S1 features an initial increase in pressure followed by a sudden drop; Stage S2 is marked by a fluctuating but slowly increasing pressure; Stage S3 shows a faster rise in pressure; and a sharp decline towards the end distinguishes Stage S4.

CT scan slices (ii to v) in Fig. 3(c) correspond to these stages. The pressure increase at the first stage is caused by gas compression within the injection tube, and the pressure sudden drop occurs when the gas overcomes the capillary threshold of the injection tube (slice i to ii). Gas volume expanded during the sudden pressure drop goes into the pores. Such repetitive injection processes result in the fluctuating pattern in S2. Slice

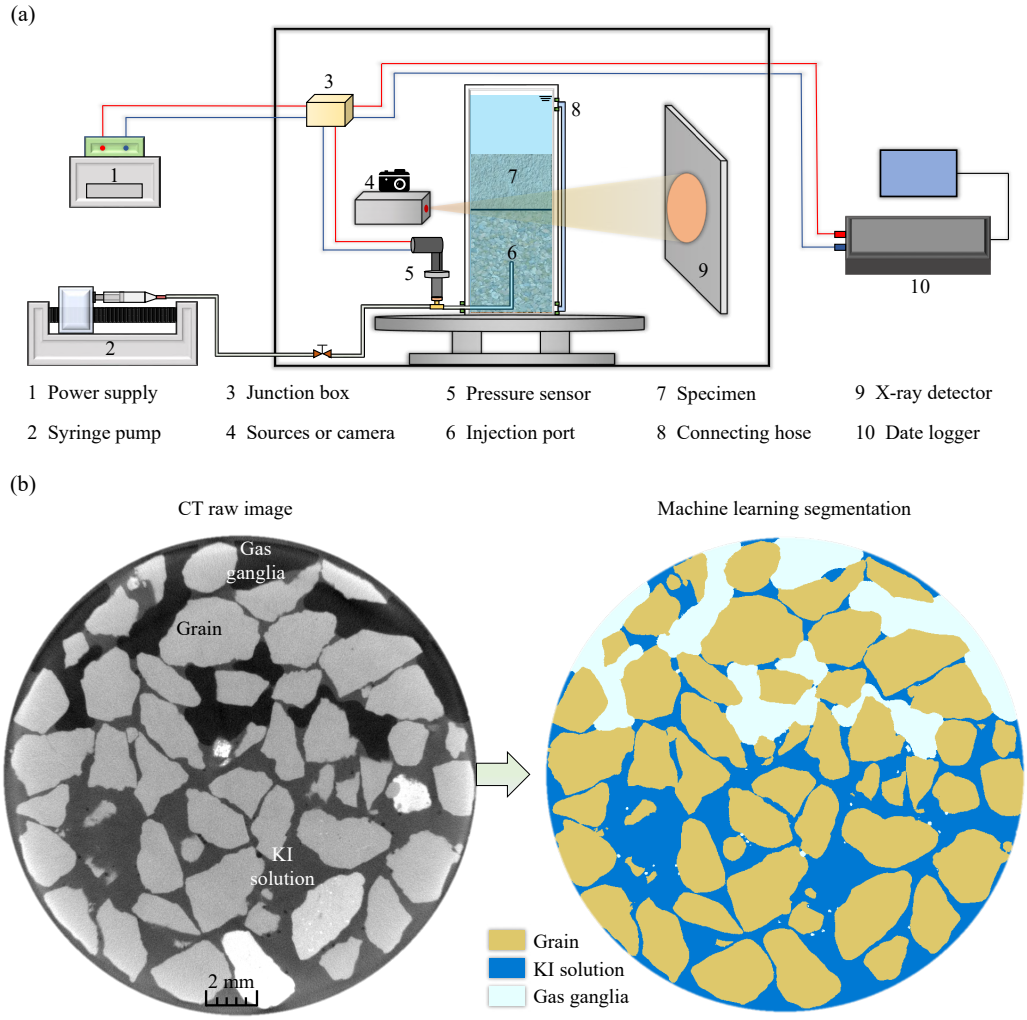

Fig. 2. Experimental setup and CT imaging. (a) The gas injection system using X-ray CT and (b) Segmentation on the right, showing grains (yellow), pore liquid (blue), and gas ganglia (white), derived from the CT raw image on the left using a machine learning algorithm.

iii shows the bubble trapping in the pore of the reservoir layer at this stage. As the progression reaches to stage S3 and slice iv, the bubbles form a connected network with a thickness H_g. Finally, the cap layer is lifted by gas at stage S4. Fig. 4(a) demonstrates the 3D gas evolution segmented from CT images. And Fig. 4(c) plots the gas saturations S_g (the ratio between gas and pore volume) in horizontal slices against the vertical slice index. From (iv) to (v), S_g gradually shifts to a uniform distribution along the vertical direction within the reservoir layer.

Under the partially-drained condition, the four stages S1 to S4 are still distinguishable in Fig. 3(b). Excess pore fluid pressure built up during gas injection cannot be neglected since the drainage has to go through the cap layer. The total injection duration is notably reduced by half; in other words, the volume of gas needed to induce cap layer failure is roughly half of the drained condition. The pressure variation rates versus injected gas volume from S2 to S4 are all significantly larger than the drained condition. As shown in Fig. 3(d), from slice iv to v, the bubbles create a narrow channel and suddenly cause local lifting at the bottom of the cap layer. A non-uniform spreading along the vertical direction within the reservoir layer is demonstrated in the Fig. 4(d).

Under both conditions, the system undergoes a pressure-built-up period and a sudden release period when a barrier is overcome. The result differs from previous laboratory experiments in 2D homogeneous porous media (Sun and Santamarina, 2019; Liu et al., 2021). This cycle repeats if gas injection continues as the barrier rebuilds after the sudden release.

3.2 Effective stress analyses

Fig. 5 illustrates the variation of total stress σ, effective stress σ' and pore pressure u_w at different depths of the specimen (C1), comparing its initial state to the final stage just before failure. According to Terzaghi's effective stress principle (Terzaghi, 1943), the total stress σ in a saturated specimen is given by the following equations at the initial state:

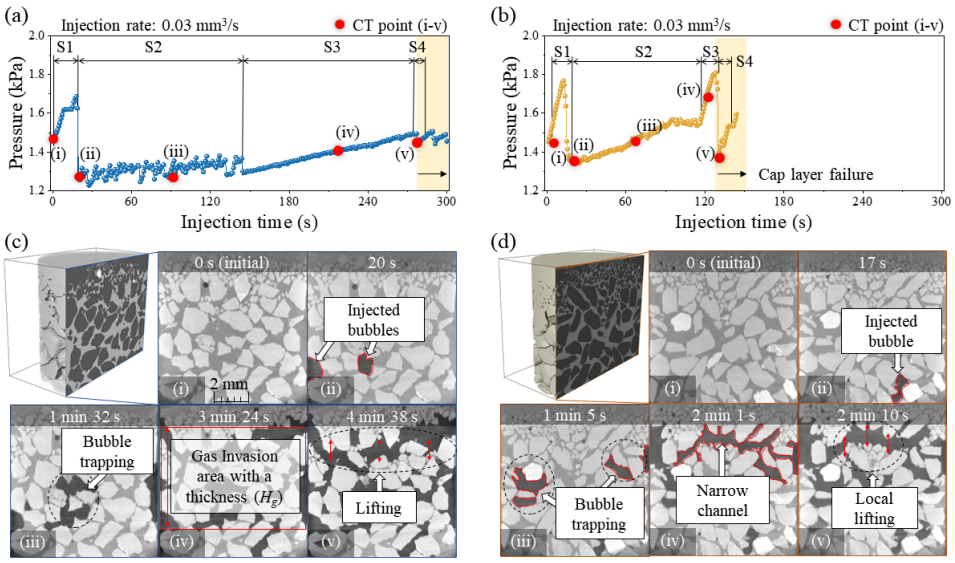

Fig. 3. System response in specimen case 1 under drained condition shown in (a) and (c), and partially-drained condition shown in (b) and (d). (a) and (b) Pressure versus injection time. (c) and (d) Vertical CT slices showing the bubble trapping and migration. The bright, gray and black phases indicate grains, pore liquid, and gas bubble. Gas initial growth and subsequent detachment in slice i to ii. During the injection process, bubbles form a gas invasion area (drained) with a thickness (H_g) or a narrow channel (partially-drained) to deform the cap layer, as seen in slice iii to v.

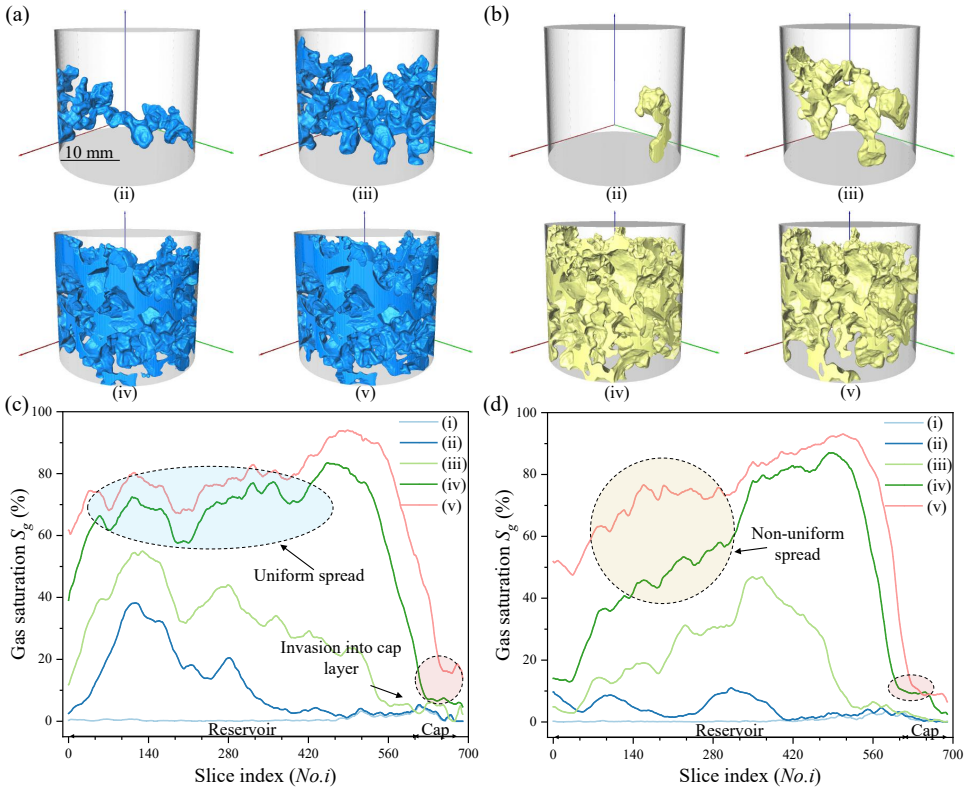

Fig. 4. Response in specimen case 1 under drained shown in (a) and (c) and partially-drained conditions shown in (b) and (d). (a) and (b) 3D bubble evolution. Particles and pore liquid are transparent. (c) and (d) Gas saturation (S_g) variation along the vertical direction. 0^{th} to 618^{th} slices correspond to the reservoir layer, and the slices above are the cap layer.

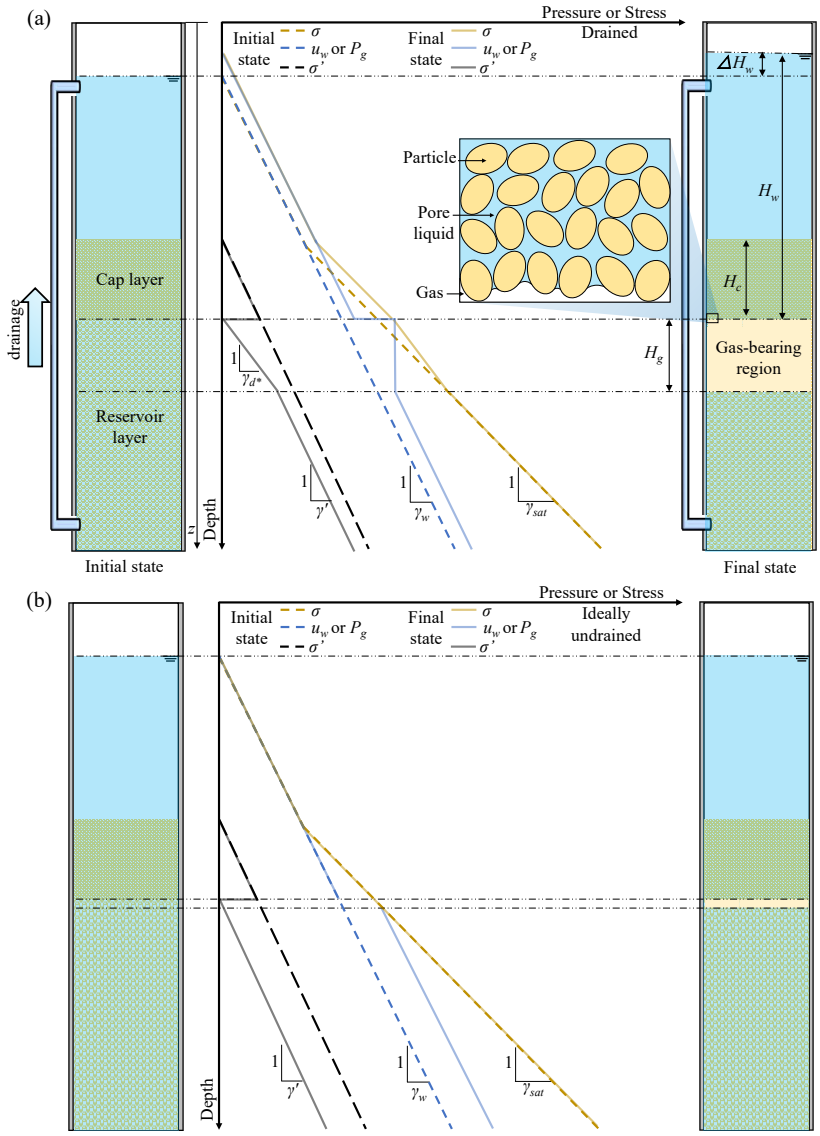

Fig. 5. Effective stress σ' varies at different depths for (a) drained and (b) ideally undrained conditions. On the left, the layer system's initial state is shown with total stress σ (depicted as a yellow dotted line), pore liquid pressure u_w (blue dotted line), and the effective stress σ' (black dotted line), with the physical meaning of their slopes represented by γ_{sat}, γ_w, and γ'. On the right, the final state preceding the cap layer's uplifting failure is depicted.

$$\begin{aligned} \sigma &= \sigma' + u_w = \gamma_{sat} z \\ u_w &= \gamma_w z \\ \sigma' &= \gamma' z \end{aligned} \tag{1}$$

where γ_{sat} is the saturated unit weight, γ_w is the water unit weight, γ' is the buoyant unit weight, and z is the depth of the specimen.

Just before the cap layer is lifted, the gas layer thickness increases to H_g, as mentioned in Section 3.1 (Fig. 5(a)). Here, the thickness H_g refers to the vertical range of the gas phase within the pores of the reservoir layer under drained conditions (disregarding sidewall friction of the cap layer). Just before the uplifting of the cap layer, the equilibrium among particles, pore liquid, and gas bubbles can be described as follows:

$$P_g = u_w + \sigma' \tag{2}$$

where P_g is the gas pressure at the top of the reservoir layer:

$$P_g = \gamma_w (H_w + H_g) - \rho_g g H_g + P_c \tag{3}$$

Since the capillarity in the reservoir layer P_c can be neglected and the same applies for gas density in this study, the equation could be simplified to:

$$P_g = \gamma_w (H_w + H_g) \tag{4}$$

$$u_w = \gamma_w H_w \tag{5}$$

$$\sigma' = \gamma' H_c \tag{6}$$

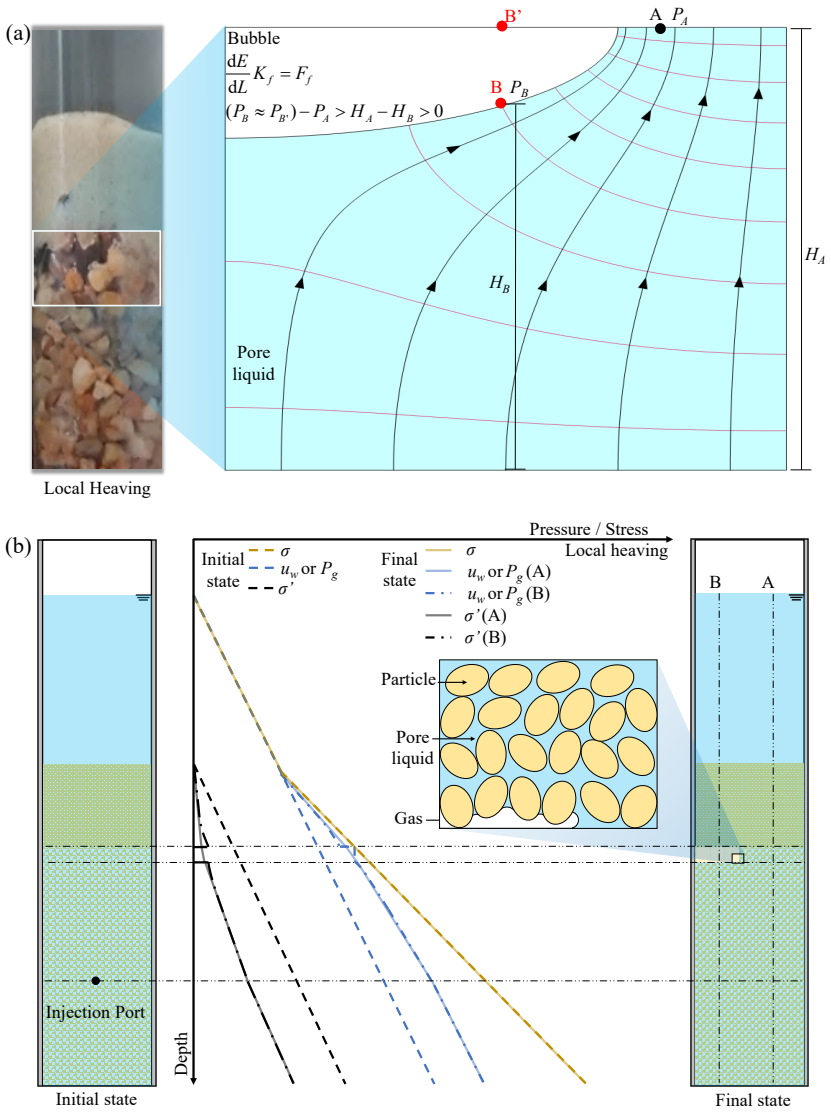

Fig. 6. (a) Hydraulic and (b) effective stress analysis of the local heaving. In the hydraulic analysis, the white and blue regions in the right denote gas bubbles and pore liquid saturated reservoir region. Black arrows delineate the flow lines. The red dashed lines define the equipotential surfaces.

where H_w is the water head above the gas zone, H_c is the thickness of the cap layer. γ' with a magnitude of ap proximately 1.2 g/cm^3 $\approx$ 1.2 γ_w in this study, and g is the gravitational acceleration. It is then interesting to see the gas zone thickness is roughly 1.2 times the thickness of the cap layer, $H_g \approx 1.2H_f$, which agrees well with experimental observations.

Meanwhile, u_w increases due to the displacement by gas, which raises the water head by ΔH_w ($\Delta H_w = H_g * n_g$, where n_g equals gas saturation S_g times the porosity n of the reservoir layer). The gas pressure equals the water pressure at the bottom of the gas layer, as capillarity in the reservoir layer is neglected. Then, the difference between gas pressure and water pressure, also the capillarity, at the bottom of the cap layer increases with H_g, that is $P_c = (\rho_L - \rho_G) g H_g$. When the capillarity exceeds the effective stress, gas uplifts the cap layer.

Fig. 5(b) illustrates an ideal undrained condition where a thin layer of gas separates the pore water in the cap and reservoir layers and pore water cannot escape. Water head and total stress remain in the cap layer. Both gas and water pressure in the reservoir increases, reducing the effective stress at the top of the reservoir layer, and the cap layer is uplifted when this effective stress decreases to zero.

3.3 Excess pore fluid pressure during fast injection

Actual gas injection in geological settings could be pulsed and fast (Ali et al., 2022), as indicated in observations from our experiments: A pulse of injection occurs when a barrier such as capillarity is broken by the accumulated gas pressure. Fast injection combined with limited drainage leads to excess pore fluid pressure Δu, which could also overcome the effective stress and cause sediment skeleton failure. Since pore fluid pressure dissipates through uniform upward water flow, Δu

could be calculated by Darcy's law:

$$\frac{Q_{out}\mu L}{kA} = \Delta u \tag{7}$$

where Q_{out} is the vertical water flow rate, A and k are the cross-sectional area, and permeability in the cap layer, and μ is fluid viscosity. k and an averaged Q are measured in the experiments (Detailed in Supplementary file, Table S1).

When the injection rate increases and the cap layer is less permeable, excess pore fluid pressure can exceed the effective stress and induce liquefaction. Such an analyses applies if water is injected. However, when gas is injected, new behaviors emerge. In an extreme case, when water flow totally lifts the particles, the cap layer behaves like liquid, and bubbles in such a system could displace the particles without invading into the pores even in coarse sediments where $P_c^* < \sigma'$. Therefore, fractures are observed in all specimens when excess pore fluid pressure exceeds the effective stress. As gas injection rate increases further, local heaving occurs after fracturing in relatively fine cap layers.

Fig. 6 shows the mechanical analyses during local heaving. As the accumulated gas bubbles, trapped by capillarity, obstructs the drainage pathways, fluid flow concentrates in a local area. The distribution of fluid flow nets is plotted (depicted as solid black lines, with arrows denoting flow direction) surrounding the bubbles. The black arrows depict the flow lines of the fluid. These lines indicate the path that the fluid would take as it flows through the layered system. The red dashed lines represent equipotential lines. Along these lines, the total hydraulic head is constant, or the fluid pressure plus the elevation head is the same at all points along a given red dashed line. A simple analysis yields that the fluid pressure at point B' is always larger than at point A, which induces a local heaving on top of the gas bubble (Fig. 6(a)):

$$\frac{\mathrm{d}E}{\mathrm{d}L}K_f = F_f \tag{8}$$

where $\mathrm{d}E > 0$ because the flow F_f is positive, and dE between points A and B can be described as, Therefore, $P_B = P_{B'} > P_A$. So, the heaving would occur above the bubbles:

$$\mathrm{d}E = (P_B + H_B) - (P_A + H_A) > 0 \tag{9}$$

When gas injection rate increases further, violent liquefaction occurs and totally destroys the initial fabric of the cap layer. Fig. 6(b) shows the mechanical response of the system during local heaving. The slope of the pore fluid pressure on the saturated side reflects the local permeability and flow line concentration. There is a sudden jump in pore fluid pressure just beneath the cap layer, which is held by capillarity. The excess pore fluid pressure works together with the capillarity on top of the gas bubble against effective stress to locally lift the cap layer.

3.4 Phase diagram for failure patterns

Two dimensionless parameters are defined at the bottom of the cap layer: $\chi_{C/R}$ (the ratio between P_c^* and σ', a higher $\chi_{C/R}$ indicates a dominance of capillary forces) and $\chi_{E/R}$ (the ratio between Δu built up during gas injection and σ', a higher

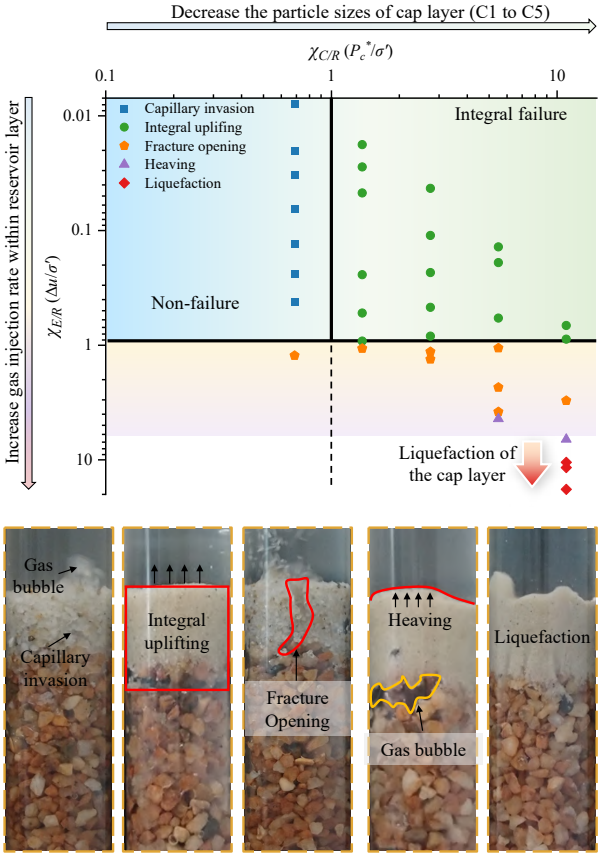

Fig. 7. Phase diagram of the five failure patterns separated by dimensionless parameters. Three failure regions are divided by the boundary of $\chi_{C/E} = 1$ and $\chi_{E/E} = 1$. Different failure patterns observed in 50 experiments are marked with color points. Below are screenshots.

$\chi_{E/R}$ suggests significant excess pore pressure, potentially causing particle deformation). These two parameters differentiate two causes for cap layer failure: Capillarity or excess pore fluid pressure. P_c^* is measured by the capillary rise height in different cap layers, and σ' is calculated based on their thickness L.

Two boundaries, $\chi_{C/R} = 1$ and $\chi_{E/R} = 1$, separate the diagram in Fig. 7 into three sections: Non-failure, integral failure and localized failure of the cap layer. In the non-failure region ($\chi_{C/R} < 1$ and $\chi_{E/R} < 1$), P_c^* and Δu at the bottom of the cap layer are both lower than σ'. Here, as gas bubbles migrate towards the cap layer base and form a gas layer, the low capillary barrier allows the gas to invade into the cap layer before causing failures of the cap layer. This process is known as capillary invasion (effective stress analysis in Supplementary file, Fig. S1).

As particle size in the cap layer decreases, the failure pattern transitions into the integral failure ($\chi_{C/R} > 1$ and $\chi_{E/R} < 1$). Under this condition, gas cannot penetrate the capillary barrier, resulting in gas accumulation within the reservoir. Eventually, the bubbles form a continuous gas zone (as mentioned Section 3.1) under a low Δu, leading to the integral lifting of the entire cap layer.

When $\chi_{E/R} > 1$, excess pore fluid pressure built up during

the injection exceeds the effective stress. As the accumulated gas bubble is not enough to form an evenly distributed gas zone, the cap layer failure is often localized. In this high Δu region, the role of P_c^* is weakened, and effect of particle size is mainly in determining the permeability, which influences the pore pressure dissipation rate. As discussed in the previous section, as gas injection rates increases, the failure shifts from local fracturing in all specimens ($7 > \chi_{E/R} > 1$), to subsequent local heaving ($10 > \chi_{E/R} > 7$, and $\chi_{C/R} > 1$), and to violent liquefaction ($\chi_{E/R} > 7$).

3.5 Implication and limitation

Geological settings predominantly contain multiple layers, most of which could be considered as a stacking of multiple two-layer systems with different layer thickness, pore size, effective stress lever and gas injection rate (Huppert and Neufeld, 2014; Ali et al., 2022; Blunt and Lin, 2022). The breakthrough of one cap layer could be the gas source injected to the adjacent reservoir layer just above the cap layer. Then, the different stages with pressure built up and sudden releases apply universally.

The phase diagram, constructed from dimensionless parameters, is universal and can be applied to any systems with similar settings. Obviously, these conclusions could be used to explain observations in shallow systems such as pockmarks and gas seeps. In a deeper environment, the pore size should decrease to maintain the same $\chi_{C/R}$ ratio between capillary barrier and effective stress, which can correspond to a deep shale formation as the cap layer. For the other ratio $\chi_{E/R}$, as the drainage path, like effective stress, also increases linearly with the depth, $\chi_{E/R}$ does not change if the thickness of the cap layer increases, therefore, the critical injection rate causing cap layer deformation could remain the same as that in shallow systems. If one conducts safety analyses for a certain reservoir during operation and long term storage, all failure patterns should be considered. From another point of view, this phase diagram provides a criterion to analyze the gas storage capacity, which is closely related to the gas layer thickness as shown in Fig. 5.

Our experimental work is constrained by certain assumptions, which include the following:

1) The simplified nature of our specimen may not fully capture the complexity of real geological formations, particularly in terms of layer anisotropy (Fishbaugh et al., 2010);
2) The analysis here is conservative because the tensile strength of the geological formations is not considered;
3) The effective stress analysis assumes linear changes with depth, which simplify real-world scenarios that involve nonlinear processes and variations along direction (Guerriero and Mazzoli, 2021).

4. Conclusions

This study employs X-ray imaging to observe gas invasion and the subsequent particle failure patterns within a layered porous media system. The system comprises a bottom reservoir layer, characterized by coarse sand exhibiting negligible capillary pressure effects, and a cap layer, composed of fine sand with various particle sizes. Salient conclusions follow:

1) The gas invasion in a layered system is featured by cycles of pressure built up and sudden release when a barrier, either capillarity P_c^* or effective stress σ' is overcome.
2) Drainage conditions significantly affect the trapped gas volume and effective stress variation within the reservoir layer. Under drained condition, the key interplay is between characterized capillarity and effective stress. While under partially-drained condition, excess pore fluid pressure Δu becomes an element that cannot be ignored, and the interplay is between effective stress and the sum of capillarity and Δu.
3) Excess pore fluid pressure Δu accumulates during rapid gas injection. This Δu, when combined with non-uniform migration of gas bubbles, leads to localized failure of the cap layer.
4) The failure patterns of the cap layer are determined by two dimensionless parameters, $\chi_{C/R}(P_c^*/\sigma')$ and $\chi_{E/R}(\Delta u/\sigma')$. When $\chi_{C/R} < 1$ and $\chi_{E/R} < 1$, the cap layer does not deform, termed capillary invasion. Integral uplifting occurs if $\chi_{C/R} > 1$ and $\chi_{E/R} < 1$. When $\chi_{E/R} > 1$, localized failure is observed, leading to fractures ($7 > \chi_{E/R} > 1$) or local heaving ($10 > \chi_{E/R} > 7$, and $\chi_{CER} > 1$). Violent liquefaction in the cap layer occurs when $\chi_{E/R} > 10$.

These findings, based on dimensionless analyses, are believed to be universal and could therefore be applied to various practices with similar settings, such as gassy sediments, pockmark formation, and geological CO_2 sequestration. Future studies could explore the interactions between different types of porous media layers in more detail. This includes investigating how variations in layer composition and fluid properties affect gas migration and trapping mechanisms under varying pressure and temperature conditions.

Acknowledgements

This work is supported by Research Center for Industries of the Future (RCIF), Westlake Education Foundation, and Open Research Fund of State Key Laboratory of Geomechanics and Geotechnical Engineering, Institute of Rock and Soil Mechanics, Chinese Academy of Sciences (No. SKLGME021008).

Conflict of interest

The authors declare no competing interest.

References

Ali, M., Jha, N. K., Pal, N., et al. Recent advances in carbon dioxide geological storage, experimental procedures, influencing parameters, and future outlook. Earth-Science Reviews, 2022, 225: 103895.

Barry, M., Boudreau, B., Johnson, B., et al. First-order de-

scription of the mechanical fracture behavior of fine-grained surficial marine sediments during gas bubble growth. Journal of Geophysical Research: Earth Surface, 2010, 115: F04029.

Blunt, M. J. Multiphase Flow in Permeable Media: A Pore-scale Perspective. Cornwall, UK, Cambridge University Press, 2017.

Blunt, M. J., Lin, Q. Flow in porous media in the energy transition. Engineering, 2022, 14: 10-14.

Brooks, J. M., Cox, H. B., Bryant, W. R., et al. Association of gas hydrates and oil seepage in the Gulf of Mexico. Organic Geochemistry, 1986, 10: 221-234.

Cai, J., Jin, T., Kou, J., et al. Lucas–Washburn equation-based modeling of capillary-driven flow in porous systems. Langmuir, 2021, 37: 1623-1636.

Cai, J., Zhao, J., Zhong, J., et al. Microfluidic experiments and numerical simulation methods of pore-scale multiphase flow. Capillarity, 2024, 12(1): 1-5.

Campbell, J. M., Ozturk, D., Sandnes, B. Gas-driven fracturing of saturated granular media. Physical Review Applied, 2017, 8: 064029.

Chevalier, C., Lindner, A., Leroux, M., et al. Morphodynamics during air injection into a confined granular suspension. Journal of Non-Newtonian Fluid Mechanics, 2009, 158: 63-72.

Chiu, J. K., Tseng, W. H., Liu, C. S. Distribution of gassy sediments and mud volcanoes offshore southwestern Taiwan. TAO: Terrestrial, Atmospheric and Oceanic Sciences, 2006, 17: 703.

Choi, J. H., Seol, Y., Boswell, R., et al. X-ray computed-tomography imaging of gas migration in water-saturated sediments: From capillary invasion to conduit opening. Geophysical Research Letters, 2011, 38: L17310.

Espinoza, D. N., Santamarina, J. C. Water-CO_2-mineral systems: Interfacial tension, contact angle, and diffusion—Implications to CO_2 geological storage. Water Resources Research, 2010, 46: W07537.

Eyinla, D. S., Leggett, S., Badrouchi, F., et al. A comprehensive review of the potential of rock properties alteration during CO_2 injection for EOR and storage. Fuel, 2023, 353: 129219.

Fauria, K. E., Rempel, A. W. Gas invasion into water-saturated, unconsolidated porous media: Implications for gas hydrate reservoirs. Earth and Planetary Science Letters, 2011, 312: 188-193.

Ferer, M., Ji, C., Bromhal, G. S., et al. Crossover from capillary fingering to viscous fingering for immiscible unstable flow: Experiment and modeling. Physical Review E, 2004, 70: 016303.

Fernández, J. F., Rangel, R., Rivero, J. Crossover length from invasion percolation to diffusion-limited aggregation in porous media. Physical Review Letters, 1991, 67: 2958.

Fishbaugh, K. E., Byrne, S., Herkenhoff, K. E., et al. Evaluating the meaning of "layer" in the Martian north polar layered deposits and the impact on the climate connection. Icarus, 2010, 205: 269-282.

Guerriero, V., Mazzoli, S. Theory of effective stress in soil and rock and implications for fracturing processes: A review. Geosciences, 2021, 11: 119.

Hematpur, H., Abdollahi, R., Rostami, S., et al. Review of underground hydrogen storage: Concepts and challenges. Advances in Geo-Energy Research, 2023, 7(2): 111-131.

Holtzman, R., Szulczewski, M. L., Juanes, R. Capillary fracturing in granular media. Physical Review Letters, 2012, 108: 264504.

Hovland, M. Hydrocarbon seeps in northern marine waters: Their occurrence and effects. Palaios, 1992, 7(4): 376-382.

Huang, H., Zhang, F., Callahan, P., et al. Fluid injection experiments in 2D porous media. SPE Journal, 2012, 17(3): 903-911.

Huppert, H. E., Neufeld, J. A. The fluid mechanics of carbon dioxide sequestration. Annual Review of Fluid Mechanics, 2014, 46: 255-272.

Hustoft, S., Mienert, J., Bünz, S., et al. High-resolution 3D-seismic data indicate focussed fluid migration pathways above polygonal fault systems of the mid-Norwegian margin. Marine Geology, 2007, 245: 89-106.

Jain, A., Juanes, R. Preferential mode of gas invasion in sediments: Grain-scale mechanistic model of coupled multiphase fluid flow and sediment mechanics. Journal of Geophysical Research: Solid Earth, 2009, 114: B08101.

Lei, L., Seol, Y., Jarvis, K. Pore-scale visualization of methane hydrate-bearing sediments with micro-CT. Geophysical Research Letters, 2018, 45: 5417-5426.

Lenormand, R., Touboul, E., Zarcone, C. Numerical models and experiments on immiscible displacements in porous media. Journal of Fluid Mechanics, 1988, 189: 165-187.

Li, J., Cai, J. Quantitative characterization of fluid occurrence in shale reservoirs. Advances in Geo-Energy Research, 2023, 9(3): 146-151.

Liu, H., Valocchi, A. J., Kang, Q., et al. Pore-scale simulations of gas displacing liquid in a homogeneous pore network using the lattice Boltzmann method. Transport in Porous Media, 2013, 99: 555-580.

Liu, Z., Sun, Y., Guo, W., et al. Experimental study of the characteristics of gas-injection barrier in 2D porous media. Journal of Hydrology, 2021, 593: 125919.

Lu, Y., Luan, X., Lyu, F., et al. Seismic evidence and formation mechanism of gas hydrates in the Zhongjiannan Basin, Western margin of the South China Sea. Marine and Petroleum Geology, 2017, 84: 274-288.

Mahabadi, N., Zheng, X., Yun, T. S., et al. Gas bubble migration and trapping in porous media: Pore-scale simulation. Journal of Geophysical Research: Solid Earth, 2018, 123: 1060-1071.

Mazzini, A., Sciarra, A., Lupi, M., et al. Deep fluids migration and submarine emersion of the Kalang Anyar mud volcano (Java, Indonesia): A multidisciplinary study. Marine and Petroleum Geology, 2023, 148: 105970.

Oppenheimer, J., Rust, A. C., Cashman, K. V., et al. Gas migration regimes and outgassing in particle-rich suspensions. Frontiers in Physics, 2015, 3: 60.

Ostanin, I., Anka, Z., di Primio, R., et al. Identification of a large Upper Cretaceous polygonal fault network in the Hammerfest basin: Implications on the reactivation of

regional faulting and gas leakage dynamics, SW Barents Sea. Marine Geology, 2012, 332: 109-125.

Peacock, D. C. P., Anderson, M., Rotevatn, A., et al. The interdisciplinary use of "overpressure". Journal of Volcanology and Geothermal Research, 2017, 341: 1-5.

Phukan, R., Saha, R. Low salinity surfactant alternating gas/CO_2 flooding for enhanced oil recovery in sandstone reservoirs. Journal of Petroleum Science and Engineering, 2022, 212: 110253.

Qin, X., Xia, Y., Qiao, J., et al. Modeling of multiphase flow in low permeability porous media: Effect of wettability and pore structure properties. Journal of Rock Mechanics and Geotechnical Engineering, 2024, 16(4): 1127-1139.

Ranaee, E., Khattar, R., Inzoli, F., et al. Assessment and uncertainty quantification of onshore geological CO_2 storage capacity in China. International Journal of Greenhouse Gas Control, 2022, 121: 103804.

Reynolds, C., Krevor, S. Characterizing flow behavior for gas injection: Relative permeability of CO_2-brine and N2-water in heterogeneous rocks. Water Resources Research, 2015, 51: 9464-9489.

Rueden, C. T., Schindelin, J., Hiner, M. C., et al. ImageJ2: ImageJ for the next generation of scientific image data. BMC Bioinformatics, 2017, 18: 1-26.

Saffman, P. Viscous fingering in Hele-Shaw cells. Journal of Fluid Mechanics, 1986, 173: 73-94.

Saffman, P. G., Taylor, G. I. The penetration of a fluid into a porous medium or Hele-Shaw cell containing a more viscous liquid. Proceedings of the Royal Society of London. Series A. Mathematical and Physical Sciences, 1958, 245: 312-329.

Saintyves, B., Dauchot, O., Bouchaud, E. Bulk elastic fingering instability in hele-shaw cells. Physical Review Letters, 2013, 111: 047801.

Sandnes, B., Flekkøy, E., Knudsen, H., et al. Patterns and flow in frictional fluid dynamics. Nature Communications, 2011, 2: 288.

Shakhova, N., Semiletov, I., Gustafsson, O., et al. Current rates and mechanisms of subsea permafrost degradation in the East Siberian Arctic Shelf. Nature Communications, 2017, 8: 15872.

Sommer, C., Straehle, C., Koethe, U., et al. Ilastik: Interactive learning and segmentation toolkit. Paper Prsented at 2011 IEEE International Symposium on Biomedical Imaging: From Nano to Macro, Chicago, Illinois, 30 March-2 April, 2011.

Sultan, N., Plaza-Faverola, A., Vadakkepuliyambatta, S., et al. Impact of tides and sea-level on deep-sea Arctic methane emissions. Nature Communications, 2020, 11: 5087.

Sun, Z., Santamarina, J. C. Grain-displacive gas migration in fine-grained sediments. Journal of Geophysical Research: Solid Earth, 2019, 124: 2274-2285.

Szpak, M. T., Monteys, X., O'Reilly, S. S., et al. Occurrence, characteristics and formation mechanisms of methane generated micro-pockmarks in Dunmanus Bay, Ireland. Continental Shelf Research, 2015, 103: 45-59.

Teng, Y., Zhang, D. Long-term viability of carbon sequestration in deep-sea sediments. Science Advances, 2018, 4: eaao6588.

Terzaghi, K. Theoretical Soil Mechanics. New York, USA, John Wiley & Sons, 1943.

Toussaint, R., Løvoll, G., Méheust, Y., et al. Influence of pore-scale disorder on viscous fingering during drainage. Europhysics Letters, 2005, 71: 583.

Varas, G., Ramos, G., Géminard, J. C., et al. Flow and fracture in water-saturated, unconstrained granular beds. Frontiers in Physics, 2015, 3: 44.

Vidal-Gilbert, S., Tenthorey, E., Dewhurst, D., et al. Geomechanical analysis of the Naylor Field, Otway Basin, Australia: Implications for CO_2 injection and storage. International Journal of Greenhouse Gas Control, 2010, 4: 827-839.

Vidonish, J. E., Zygourakis, K., Masiello, C. A., et al. Thermal treatment of hydrocarbon-impacted soils: A review of technology innovation for sustainable remediation. Engineering, 2016, 2: 426-437.

Xue, Z., Tanase, D., Watanabe, J. Estimation of CO_2 saturation from time-lapse CO_2 well logging in an onshore aquifer, Nagaoka, Japan. Exploration Geophysics, 2006, 37: 19-29.

Zhang, C., Wang, Y., Kou, Z., et al. Recent research advances in enhanced CO_2 mineralization and geologic CO_2 storage. Advances in Geo-Energy Research, 2023a, 10(3): 141-145.

Zhang, L., Nowak, W., Oladyshkin, S., et al. Opportunities and challenges in CO_2 geologic utilization and storage. Advances in Geo-Energy Research, 2023b, 8(3): 141-145.

Zhou, N., Matsumoto, T., Hosokawa, T., et al. Pore-scale visualization of gas trapping in porous media by X-ray CT scanning. Flow Measurement and Instrumentation, 2010, 21: 262-267.

Zou, S., Chen, D., Kang, N., et al. An experimental investigation on the energy signature associated with multiphase flow in porous media displacement regimes. Water Resources Research, 2024, 60: W036241.